J. Math. Biol. (2012) 65:653–675
DOI 10.1007/s00285-011-0476-7

Mathematical Biology

An immersed boundary method for simulating a single axisymmetric cell growth and division

Yibao Li · Ana Yun · Junseok Kim

Received: 27 December 2010 / Revised: 29 September 2011 / Published online: 11 October 2011

Abstract For an animal cell, cytokinesis is the process by which a cell divides its cytoplasm to produce two daughter cells. We propose a new mathematical model for simulating cytokinesis. The proposed model is robust and realistic in deciding the position of the cleavage furrow and in defining the contractile force leading to cell division. We use an immersed boundary method to track the morphology of cell membrane during cytokinesis. For accurate calculation, we adaptively add and delete the immersed boundary points. We perform numerical simulations on the axisymmetric domain to have sufficient resolution and to incorporate three-dimensional effects such as anisotropic surface tension. Finally, we investigate the effects of each model parameter and compare a numerical result with the experimental data to demonstrate the efficiency and accuracy of our proposed method.

Keywords Cytokinesis · Cleavage furrow · Immersed boundary method · Axisymmetric simulation

Mathematics Subject Classification (2000) 65M50 · 65M06 · 9208

1 Introduction

Cytokinesis is the process by which an animal cell divides its cytoplasm to produce two daughter cells (Barr et al. 2007). A cell separates into two cells by the contractile ring which is formed by actin–myosin interactions. The contractile ring forms a cleavage furrow and as the ring tightens, the cleavage furrow develops further, eventually the cell is divided into two daughter cells. Cytokinesis consists of four major steps.

Y. Li · A. Yun · J. Kim (✉)
Department of Mathematics, Korea University,
Seoul 136-701, Republic of Korea
e-mail: cfdkim@korea.ac.kr

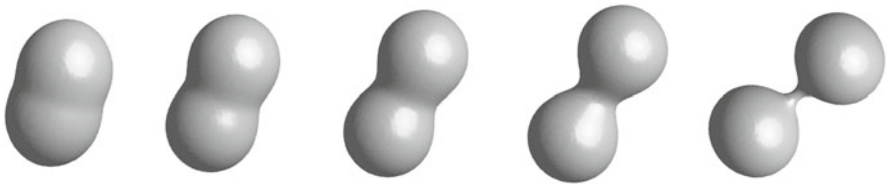

Fig. 1 Simulation of the evolution of the cytokinesis

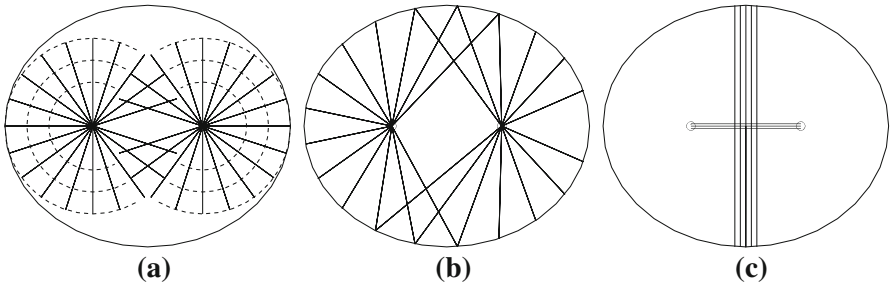

Fig. 2 Models to explain how the mitotic apparatus signals the cortex locate the cleavage furrow position. **a** Astral relaxation by signals from the astral centers. **b** Astral stimulation. **c** Equatorial stimulation by signals from the spindle midzone

The first step is to decide the position of the cleavage furrow. The second step is to form the contractile ring. The third step is contraction of the contractile ring. The final step is to break plasma membrane (Murray et al. 1983; Tyson and Hannsgen 1986; Satterwhite and Pollard 1992; Guertin et al. 2002). The physical division process of the cell is illustrated in Fig. 1.

Three models have been proposed to explain how the mitotic apparatus gives signals to the surface for deciding location of the cleavage furrow (Oegema and Mitchison 1997). The first model is the astral relaxation theory (White and Borisy 1983; Wolpert 1960) which states that signals from the asters provide relaxation of the cortex (Fig. 2a). The signals cause regional tension differences at the surface and the tension inequality causes equatorial contraction. The second model is the astral stimulation theory (Rappaport 1986; Devore et al. 1989). This model states that signals from the astral centers have larger values at the overlapped equatorial positions (Fig. 2b). The division mechanism is formed by direct response in the stimulated region. The third model suggests that an equatorial stimulation is caused by signals from the spindle midzone. In this model, the signals arise from the spindle midzone rather than the asters (Fig. 2c).

This study is a generalization and extension of the previous research by Rejniak (2005) and includes the following salient features: (a) three-dimensional axisymmetric model; (b) robust and realistic model for positioning the cleavage furrow and for defining the contractile force leading to cell division; and (c) accurate immersed boundary method. We choose the astral relaxation theory as a signal model and propose a robust and accurate mathematical model for the relaxation theory.

This paper is organized as follows. In Sect. 2, we propose our governing equations for an animal cell growth and division. In Sect. 3, the numerical method with the

adaptive immersed boundary points is given. In Sect. 4, we present numerical results such as convergence of the scheme, effects of model parameters, and comparison with the experimental data. Finally, conclusions are made in Sect. 5.

2 Mathematical formulation

Our mathematical model is based on the immersed boundary method for the cell growth and division (Rejniak 2005). The materials inside and outside of the cell are modeled as homogeneous continuum fluids (Greenspan 1977) with the same constant density ρ and viscosity μ. Two discrete material points $\boldsymbol{Y}_1$ and $\boldsymbol{Y}_2$ represent the aster centers where sources of fluid $S_1(t)$ and $S_2(t)$ are located. When $S_1(t)$ and $S_2(t)$ are positive, the cell is growing. Once the cell doubles its volume, the sources are deactivated. After that, the division site of the cell is chosen and the cleavage furrow is developed. Now, we introduce the three-dimensional governing equation for the cell evolution, then we will change it into the axisymmetric system.

$$\rho\left(\frac{\partial \boldsymbol{u}(\boldsymbol{x},t)}{\partial t}+\boldsymbol{u}(\boldsymbol{x},t)\cdot\nabla\boldsymbol{u}(\boldsymbol{x},t)\right)=-\nabla p(\boldsymbol{x},t)+\mu\Delta\boldsymbol{u}(\boldsymbol{x},t) \\ +\left(\zeta+\frac{\mu}{3}\right)\nabla(\nabla\cdot\boldsymbol{u}(\boldsymbol{x},t))+\boldsymbol{F}(\boldsymbol{x},t), \tag{1}$$

where $\boldsymbol{u}=(u,v,w)$ is the velocity, p is the pressure, and $\boldsymbol{F}=(F_1,F_2,F_3)$ is the external force density from the cell membrane. $\boldsymbol{x}=(x,y,z)$ and t are space and time coordinates, respectively. When the compressible effects of the fluid flow are negligible, ζ disappears. Also, if we have a source term for the fluid, we have the following continuity equation for the mass

$$\frac{\partial\rho}{\partial t}+\nabla\cdot(\rho\boldsymbol{u}(\boldsymbol{x},t))=S(\boldsymbol{x},t),$$

where S is the fluid source distribution (Guyon et al. 2001). Since we assume that ρ is constant, we have

$$\rho\nabla\cdot\boldsymbol{u}(\boldsymbol{x},t)=S(\boldsymbol{x},t).$$

In the axisymmetric formulation, we set $\boldsymbol{u}=(u,w)$, $\boldsymbol{F}=(F_1,F_2)$, and $\boldsymbol{x}=(r,z)$. The immersed boundary for the cell membrane is described by the function $\boldsymbol{X}(s,t)=(R(s,t),Z(s,t))$, where $0\le s\le L$ and L is the length of the boundary (see Fig. 3). Then, the axisymmetric governing equation is given as

$$\rho(u_t+uu_r+wu_z)=-p_r+\mu\left[\frac{1}{r}(ru_r)_r+u_{zz}-\frac{u}{r^2}\right]+\frac{\mu}{3\rho}S_r+F_1, \tag{2}$$

$$\rho(w_t+uw_r+ww_z)=-p_z+\mu\left[\frac{1}{r}(rw_r)_r+w_{zz}\right]+\frac{\mu}{3\rho}S_z+F_2, \tag{3}$$

$$\rho\nabla\cdot\boldsymbol{u}(\boldsymbol{x},t)=S(\boldsymbol{x},t), \tag{4}$$

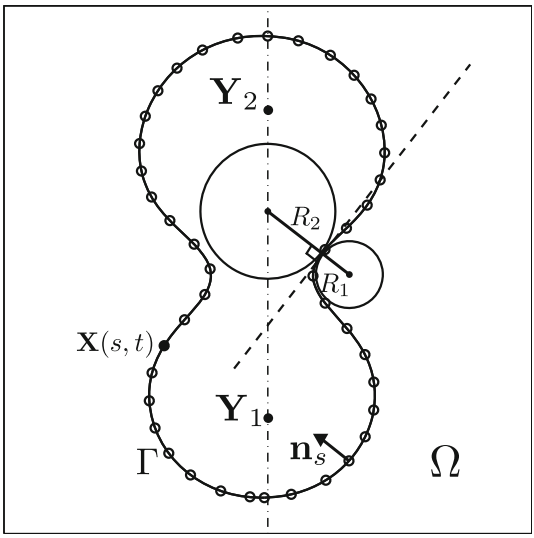

Fig. 3 Schematic of computational configuration

$$S(\boldsymbol{x},t)=\sum_{j=1}^{2}S_j(t)\delta^2(\boldsymbol{x}-\boldsymbol{Y}_j(t)), \tag{5}$$

$$S_j(t)=\varsigma(1-H(t-t_0)), \tag{6}$$

$$\boldsymbol{F}(\boldsymbol{x},t)=\int_{\Gamma}\boldsymbol{f}(s,t)\delta^2(\boldsymbol{x}-\boldsymbol{X}(s,t))ds, \tag{7}$$

$$\boldsymbol{U}(\boldsymbol{X}(s,t),t)=\int_{\Omega}\boldsymbol{u}(\boldsymbol{x},t)\delta^2(\boldsymbol{x}-\boldsymbol{X}(s,t))dx, \tag{8}$$

$$\frac{\partial\boldsymbol{X}(s,t)}{\partial t}=\boldsymbol{U}(\boldsymbol{X}(s,t),t), \tag{9}$$

$$\boldsymbol{U}(\boldsymbol{Y}_j(t),t)=\int_{\Omega}\boldsymbol{u}(\boldsymbol{x},t)\delta^2(\boldsymbol{x}-\boldsymbol{Y}_j(t))d\boldsymbol{x}\quad\text{for } j=1,2, \tag{10}$$

$$\frac{\partial\boldsymbol{Y}_j(t)}{\partial t}=\boldsymbol{U}(\boldsymbol{Y}_j(t),t), \tag{11}$$

$$\boldsymbol{f}(s,t)=\left(\frac{\sigma_1}{R_1}+\frac{\sigma_2(s,t)}{R_2}\right)\boldsymbol{n}_s=(\sigma_1\kappa_1+\sigma_2(s,t)\kappa_2)\,\boldsymbol{n}_s, \tag{12}$$

$$\kappa_1=\frac{R_sZ_{ss}-R_{ss}Z_s}{\sqrt{R_s^2+Z_s^2}^3},\quad \kappa_2=\frac{Z_s}{R\sqrt{R_s^2+Z_s^2}}, \tag{13}$$

$$\sigma_2(s,t)=\frac{\alpha H(t-t_0)}{s(\boldsymbol{X})}+\sigma_1(1-H(t-t_0)), \tag{14}$$

where ς is the positive value and $H(t)$ is the Heaviside function, where $H(t)=1$ for $t\geq 0$, and $H(t)=0$, otherwise. The time dependent source $S_j(t)$ in Eq. (6) is ς when $t<t_0$ and $S_j(t)=0$ when $t\geq t_0$. Here, t_0 is the time when the volume of the mother cell becomes double. R_1 and R_2 are the principal radii for principal curvatures κ_1 and

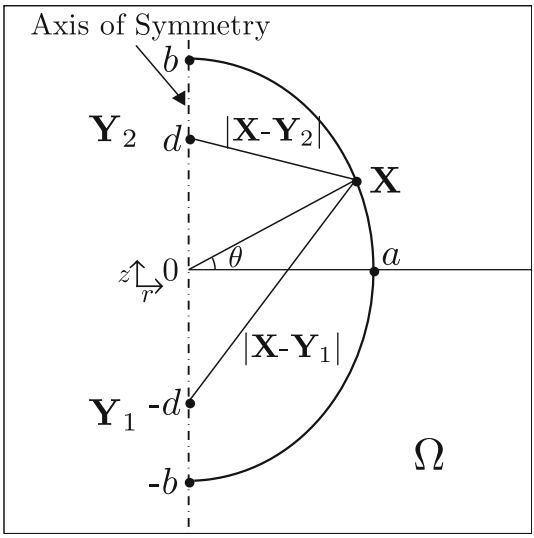

Fig. 4 Configuration of cell membrane and two astral centers

κ_2 of the cell membrane, respectively (Bernoff et al. 1998; Hilbing et al. 1995; Lai et al. 2004). $\boldsymbol{n}_s = (m_s, n_s)$ is the unit normal vector into the cell, $\sigma_1(s,t)$ and $\sigma_2(s,t)$ are stiffness coefficients for the curvature forces, and α is a scaling parameter. In Eq. (14), a time dependent surface tension σ_2 is modeled as σ_1 when $t < t_0$ and $\alpha/s(\boldsymbol{X})$ when $t \geq t_0$. Here $s(\boldsymbol{X})$ is our proposed stimulus model which will be described in the next section.

Now, we present three different previous stimulus models by White and Borisy (1983) and then we propose a more robust and realistic model. Let

$$\boldsymbol{X} = (r, z) = (a\cos(\theta), b\sin(\theta)), -\pi/2 \leq \theta \leq \pi/2$$

be the cell surface (see Fig. 4). We note that the rotated three-dimensional volume is $4a^2b\pi/3$. Two astral centers at $\boldsymbol{Y}_1 = (0, -d)$ and $\boldsymbol{Y}_2 = (0, d)$ are separated by a distance $2d$. It should be noted that we define the cell polar, located on the axis of two astral centers, and the cell equator, located orthogonal bisection to the axis of astral centers. Then, the distances from the point $\boldsymbol{X}$ on the cell membrane to the astral centers are $|\boldsymbol{X} - \boldsymbol{Y}_1|$ and $|\boldsymbol{X} - \boldsymbol{Y}_2|$.

In the previous models, the stimulus from asters is combined by simply additive way and the strength of the stimulus varies as the stimulus goes from the equator to the pole. The combined stimulus $s_i(\boldsymbol{X})$, $i = 1, 2$ and 3, follow inverse power laws as

Inverse power law: $s_1(\boldsymbol{X}) = 1/|\boldsymbol{X} - \boldsymbol{Y}_1| + 1/|\boldsymbol{X} - \boldsymbol{Y}_2|$,
Inverse square power law: $s_2(\boldsymbol{X}) = 1/|\boldsymbol{X} - \boldsymbol{Y}_1|^2 + 1/|\boldsymbol{X} - \boldsymbol{Y}_2|^2$,
Inverse fourth power law: $s_3(\boldsymbol{X}) = 1/|\boldsymbol{X} - \boldsymbol{Y}_1|^4 + 1/|\boldsymbol{X} - \boldsymbol{Y}_2|^4$.

As we will demonstrate later, these three mathematical models show different results from the astral relaxation signal model for some shapes of cells. Therefore, we need a robust model which is less sensitive to morphological type of cells. We propose a

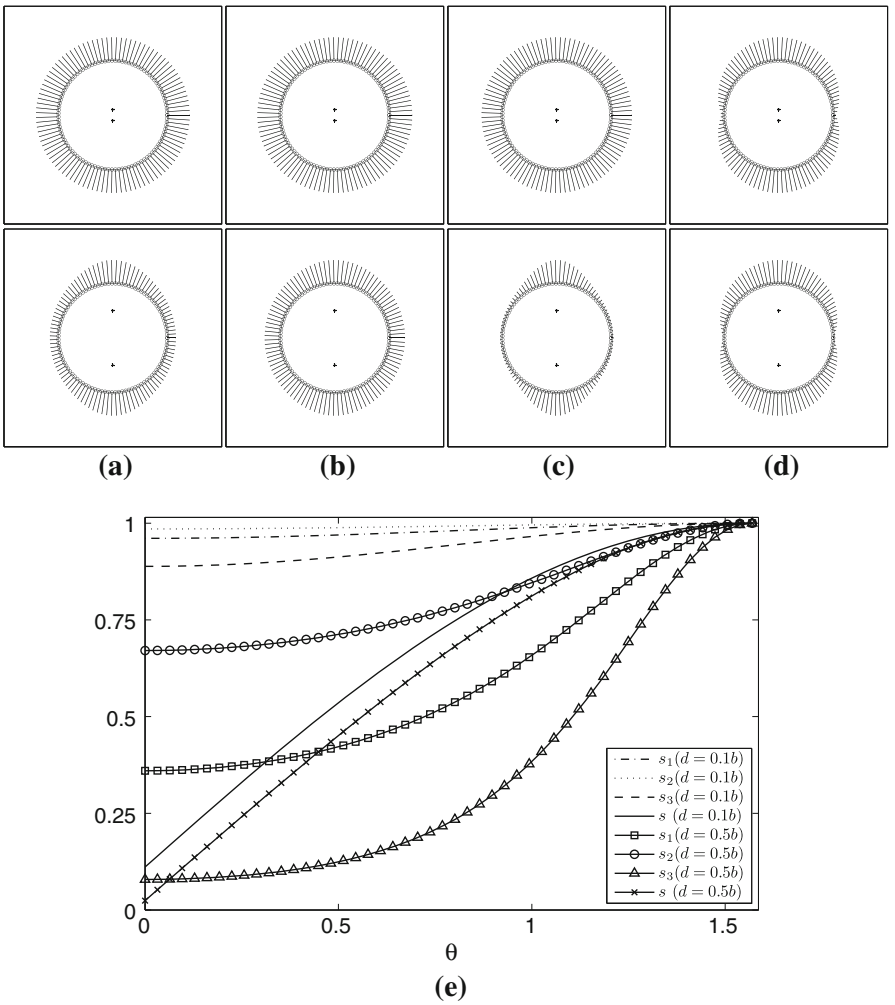

Fig. 5 Results with a spherical cell $a = b = 2$. The strength of stimulus is shown by lines drawn from the cell surface, and the symbol $*$ represent the aster centers in the *first* and the *second rows*. $d = 0.1b$ and $d = 0.5b$ are used in the *top* and *bottom rows*, respectively. **a**, **b**, **c**, and **d** are stimuli with inverse power s_1, inverse square power s_2, inverse fourth power s_3, and our proposed method s, respectively. **e** Comparison of all cases for $\theta \in [0, \pi/2]$

new mathematical stimulus model which is defined as the difference of distances from aster centers to the cell membrane and a control parameter ϵ, i.e.,

$$s(\boldsymbol{X}) = \big||\boldsymbol{X} - \boldsymbol{Y}_1| - |\boldsymbol{X} - \boldsymbol{Y}_2|\big| + \epsilon.$$

Figure 5a–d show stimulus distribution along the cell boundary with s_1, s_2, s_3, and s, respectively. Here, $a = b = 2$ and $\epsilon = 0.05$ are used. $a = b$ implies that the cell shape is a sphere. $d = 0.1b$ and $d = 0.5b$ are used in the top and bottom rows, respectively. The length of the lines drawn from the cell surface means the strength

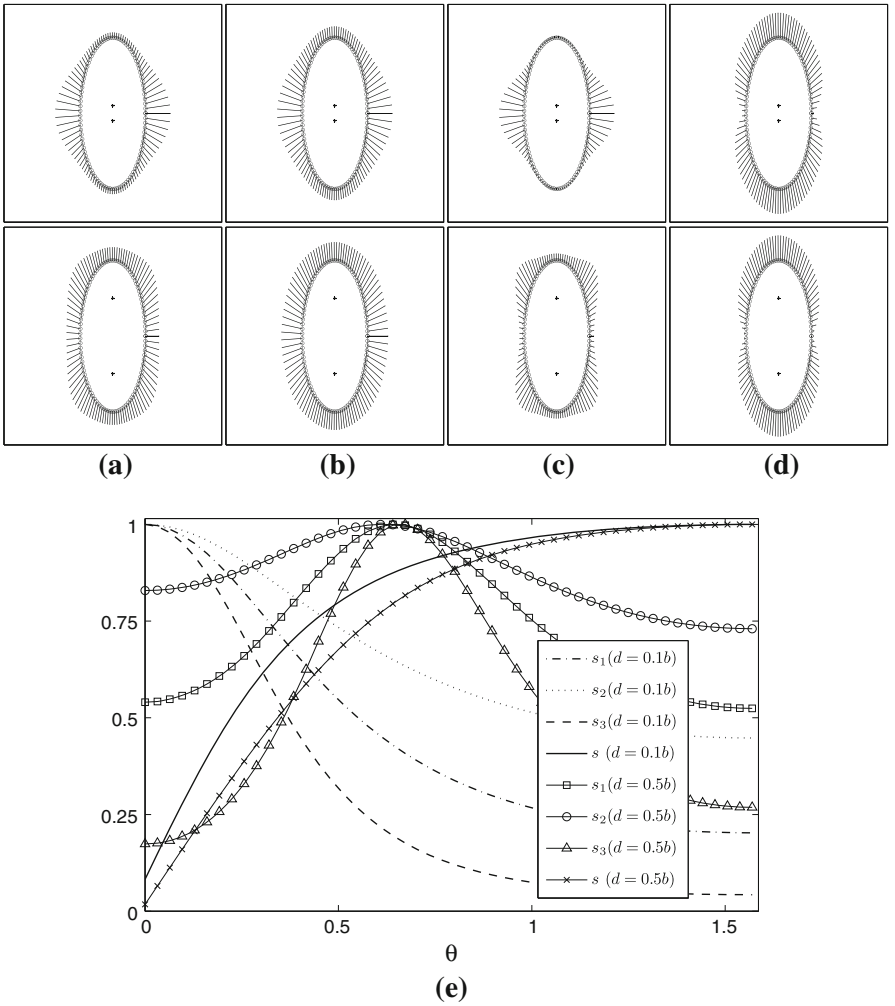

Fig. 6 Results with a non spherical cell $a = 1.2$ and $b = 2.778$. The strength of stimulus is shown by *lines* drawn from the cell surface, and the symbol $*$ represent the aster centers in the *first* and the *second rows*. $d = 0.1b$ and $d = 0.5b$ are used in the top and bottom rows, respectively. **a**, **b**, **c**, and **d** are stimuli with inverse power s_1, inverse square power s_2, inverse fourth power s_3, and our proposed method s, respectively. **e** Comparison of all cases for $\theta \in [0, \pi/2]$

of stimulus. For better comparison, we normalize the maximum strength as 1. Figure 5e shows stimulus profiles (s_1, s_2, s_3, and s) with ($d = 0.1b$ and $d = 0.5b$) for $\theta \in [0, \pi/2]$. As all cases show that the maximum strength is at the poles and the minimum strength is at the equatorial regions, these results follow well to the astral relaxation model.

Next, we consider a non spherical cell shape, i.e., $a = 1.2$ and $b = 2.778$. Figure 6a–d show stimulus distribution along the cell boundary with s_1, s_2, s_3, and s, respectively. $d = 0.1b$ and $d = 0.5b$ are used in the top and bottom rows, respectively. In Fig. 6 we can observe that all three stimulus models s_1, s_2, s_3 obtain the maximum

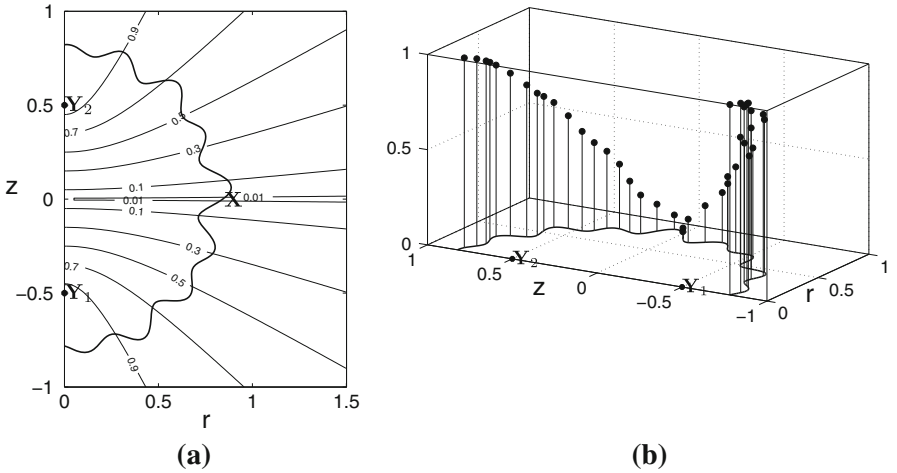

Fig. 7 **a** Contour lines of our proposed stimulus model and cell membrane. **b** Stem plot of $s(\boldsymbol{X})$

stimulus strengths at the equatorial regions and the minimum stimulus strengths at poles with $d = 0.1b$ case, and this result contradicts to the astral relaxation model. However, our proposed model has the minimum strengths at the equatorial regions and the maximum strengths at poles, regardless of the value of d. Figure 6e shows stimulus profiles with eight cases with $\theta \in [0, \pi/2]$.

From these numerical experiments, we see that our proposed signal model is less sensitive to the position of astral centers and cell shapes. Next, in order to get the explicit expression, we set a numerical experiment. Let $r(\theta)$ be a random perturbation, defined as $r(\theta) = 0.8 + \sum_{i=1}^{5} (0.015r_i \cos(20r_i\theta) + 0.03r_i \sin(20r_i\theta))$, where r_i is a random number between 0 and 1. The cell membrane $\boldsymbol{X}$ with $d = 0.5$ is shown as a thick curve in Fig. 7a. We also plot contours at levels $s = 0.01,\ 0.1,\ 0.3,\ 0.5, 0.7$ and 0.9 on the domain $\Omega = [0, 1.5] \times [-1, 1]$. As we can see from the figure, the value of s is an increasing function with respect to the absolute value of angle θ. This implies that the magnitude of $s(\mathbf{X})$ is maximum in poles and is minimum in equatorial region. In Fig. 7b, we show that the strength of $s(\mathbf{X})$ on the cell membrane by a stem plot.

For a more mathematical argument, let us consider two astral centers, $\mathbf{Y}_1 = (0, -d)$ and $\mathbf{Y}_2 = (0, d)$. Also, let the cell surface $\boldsymbol{X} = (r(\theta)\cos(\theta), r(\theta)\sin(\theta))$ have more general shapes, where $-\pi/2 \le \theta \le \pi/2$ and $r(\theta)$ is a positive valued function. For simplicity, let $\epsilon = 0$, we have

$$
\begin{aligned}
s(\boldsymbol{X}) &= \big||\boldsymbol{X} - \boldsymbol{Y}_1| - |\boldsymbol{X} - \boldsymbol{Y}_2|\big| \\
&= \big|\sqrt{(r(\theta)\cos\theta)^2 + (r(\theta)\sin\theta - d)^2} - \sqrt{\big(r(\theta)\cos\theta)^2 + (r(\theta)\sin\theta + d\big)^2}\big| \\
&= \sqrt{\Big(\sqrt{(r(\theta)\cos\theta)^2 + (r(\theta)\sin\theta - d)^2} - \sqrt{(r(\theta)\cos\theta)^2 + (r(\theta)\sin\theta + d)^2}\Big)^2} \\
&= \sqrt{2r(\theta)^2 + 2d^2 - 2\sqrt{r(\theta)^4 + d^4 + 2r(\theta)^2 d^2\cos(2\theta)}}.
\end{aligned}
$$

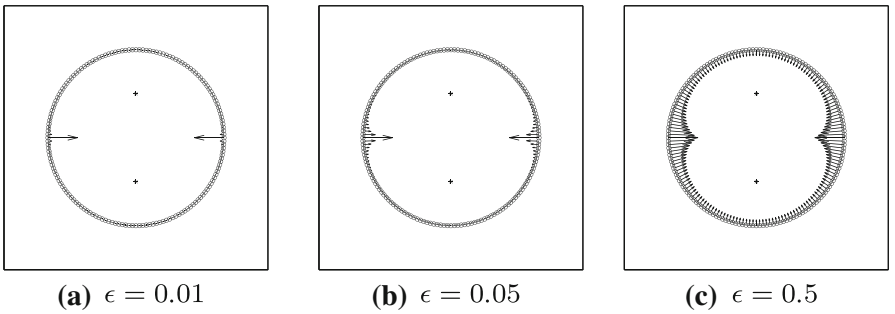

Fig. 8 Effect of ϵ values for stiffness distribution on the cell boundary

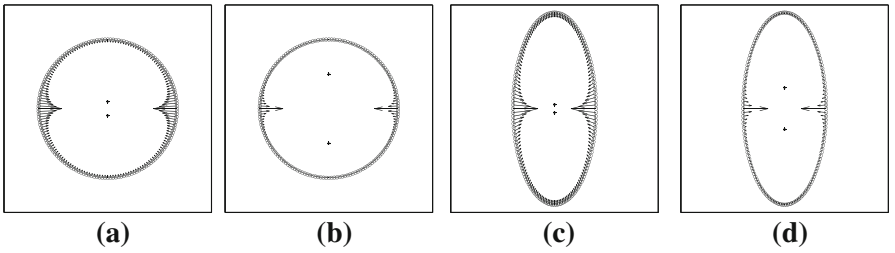

Fig. 9 Stiffness of the boundary with different shapes and aster locations. (**a**) $a = b = 2$ and $d = 0.1b$, (**b**) $a = b = 2$ and $d = 0.5b$, (**c**) $a = 1.2, b = 2.778$, and $d = 0.1b$, and (**d**) $a = 1.2, b = 2.778$ and $d = 0.5b$

Thus, if $\theta = 0$, then $s(\boldsymbol{X}) = 0$, else if $\theta = \pm\pi/2$, then $s(\boldsymbol{X}) = 2d$, otherwise, then by the triangle inequality, we get $0 < s(\boldsymbol{X}) < 2d$. Hence our proposed stimulus is minimized at the cell equator and maximized at the cell poles.

In Fig. 8, we show the effect of ϵ values ($\epsilon = 0.01,\ 0.05,\ 0.5$) for stiffness distribution on the cell boundary. We denote the magnitudes of the stimulus as arrows. The result shows that smaller ϵ value has localized high stiffness values at the equatorial regions. Figure 9 shows stiffness distribution on the cell boundary with different shapes and aster locations [(a) $a = b = 2, d = 0.1b$, (b) $a = b = 2, d = 0.5b$, (c) $a = 1.2, b = 2.778, d = 0.1b$, and (d) $a = 1.2, b = 2.778, d = 0.5b$]. We observe that the proposed stimulus works well with the different initial shapes and the positions of astral centers.

3 Numerical method

A staggered marker-and-cell (MAC) mesh of Harlow and Welch (1965) is used in which pressure is stored at cell centers and velocities are stored at cell interfaces (see Fig. 10).

We consider an axisymmetric domain $\Omega = \{(r, z) : 0 < r < R,\ -H/2 < z < H/2\}$. Let a computational domain be partitioned in Cartesian geometry into a uniform mesh with mesh spacing h. The center of each cell, Ω_{ik}, is located at $(r_i, z_k) = ((i - 0.5)h, (k - 0.5)h)$ for $i = 1, \ldots, N_r$ and $k = 1, \ldots, N_z$, where

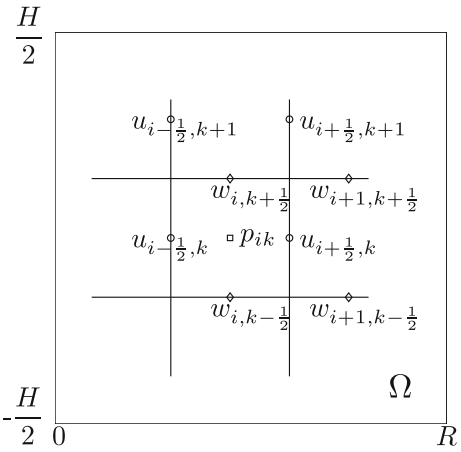

Fig. 10 Velocities are defined at cell boundaries, while the pressure field is defined at the cell centers

N_r, N_z are the numbers of cells in r, z-directions, respectively. The cell vertices are located at $(r_{i+\frac{1}{2}}, z_{k+\frac{1}{2}}) = (ih, kh)$. Then the fluid equations (2)–(4) in Eulerian form are discretized on a fixed rectangular lattice at time $t = n\Delta t$: $\boldsymbol{x}_{ik}^n = \boldsymbol{x}(r_i, z_k, n\Delta t)$, where $n = 0, 1, \ldots$. The immersed boundary equations (8)–(11) in Lagrangian form are discretized on a collection of moving points $\boldsymbol{X}_l^n = (R_l^n, Z_l^n)$ for $l = 1, \ldots, M$, and two astral centers $\boldsymbol{Y}_j^n = (R_j^n, Z_j^n)$ for $j = 1, 2$. And let $\Delta s_{l+1}^n = |\boldsymbol{X}_{l+1}^n - \boldsymbol{X}_l^n|$ be the distance between two points.

Our goal is to compute $\boldsymbol{u}^{n+1}$, $\boldsymbol{X}^{n+1}$, $\boldsymbol{Y}^{n+1}$ from given $\boldsymbol{u}^n$, $\boldsymbol{X}^n$, $\boldsymbol{Y}^n$. Detailed description for the numerical solution is described in Appendix.

4 Numerical experiments

In this section, we perform several numerical experiments such as the simulation of cell proliferation, effect of interpolation, convergence test, effect of source positions, various initial shapes, effects of viscosity μ and control parameter ϵ, and comparison of our numerical result with the experimental data. We use the units of density, viscosity, source, and surface tension in an arbitrary unit system except the test for the comparison with experiment data. We use $\varsigma = 1$, $\rho = 1$, and the number of immersed boundary points $M \approx 4L_B/h$, where L_B is the length of the initial immersed boundary. The 'final shape' of cell in our numerical experiments is defined when the distance between the cell equator to the axis is smaller than tol. Here we set $tol = 0.1$.

4.1 Cell growth

In this experiment, we use computational domain $(0, \pi) \times (-\pi, \pi)$ with 64×128 mesh grids, time step $\Delta t = 0.75h^2$, $\mu = 0.2$, $\sigma_1 = 0.05$, $\alpha = 0.02$, $\epsilon = 0.01$, $\boldsymbol{Y}_1 = (0, -0.003)$, and $\boldsymbol{Y}_2 = (0, 0.003)$ with an initial spherical shape ($a = b = 1$). A process of cell proliferation is modeled by introducing two point sources inside the cell. The sources correspond to two astral centers which are close enough to each

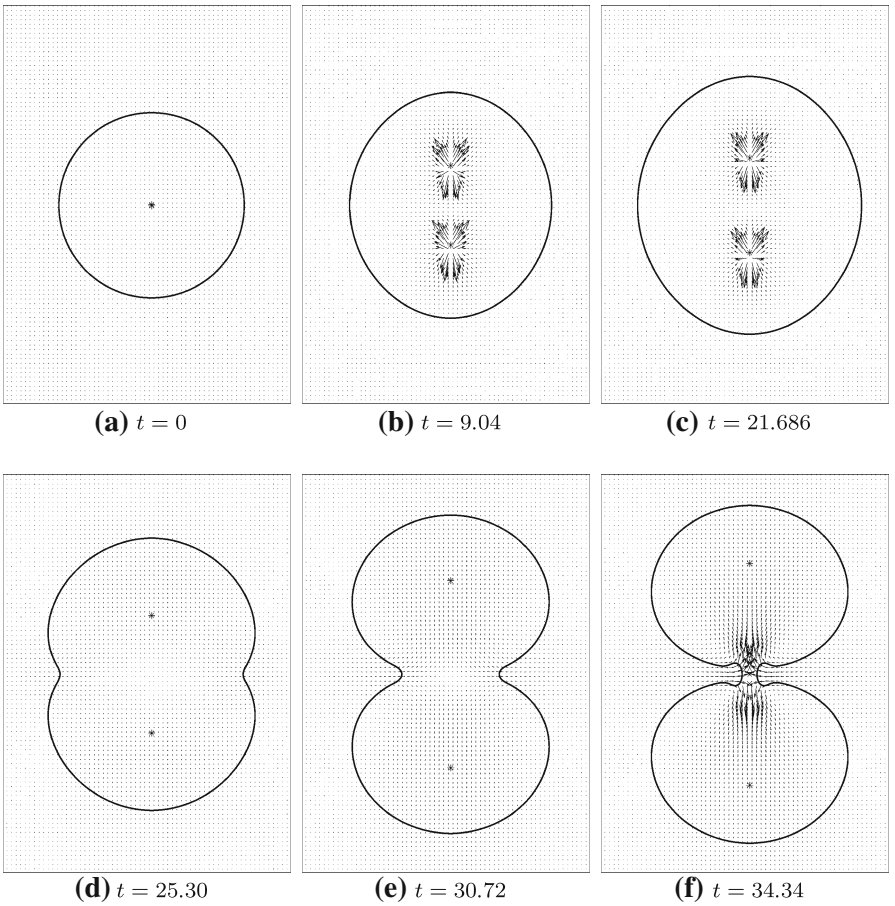

Fig. 11 Temporal evolution of cell morphology. **a** Cell ready to proliferate. **b–c** Cell growth and elongation. **d–f** Evolution of the contractile ring

other (Fig. 11a). Fluid flow created by both sources causes cell growth by pushing cell membranes (Fig. 11b–c). Here, the velocity vector field is indicated as quiver. When the volume of the cell becomes double, the sources are deactivated and the contracting force is activated. The contracting force makes cleavage furrow for actual division process (Fig. 11d–f).

4.2 Effect of interpolation

In order to study the effect of interpolation, a numerical experiment is performed on the computational domain $\Omega = (0, \pi) \times (-\pi, \pi)$ with a 64×128 grid. Here interpolation means that we add or delete immersed boundary points based on interpolation. The initial shape is given by setting $a = 1.5$ and $b = 1.0$ with $\boldsymbol{Y}_1 = (0, -0.157)$ and $\boldsymbol{Y}_2 = (0, 0.157)$. The parameters are $\mu = 0.2, \sigma_1 = 0.05, \alpha = 0.02, \epsilon = 0.01$, and

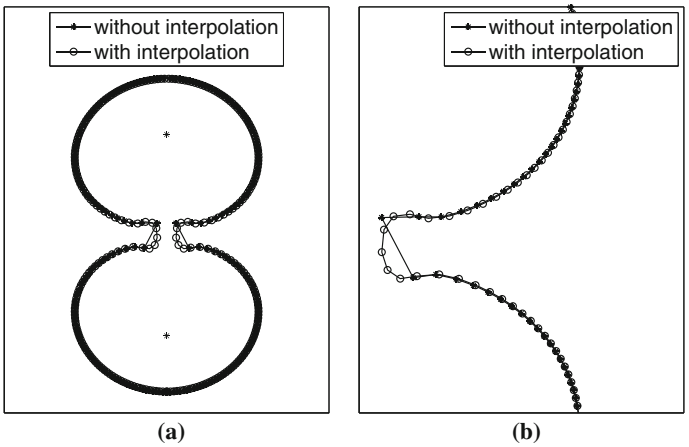

Fig. 12 **a** The comparison of cell growth simulation with and without interpolations. **b** Closeup view

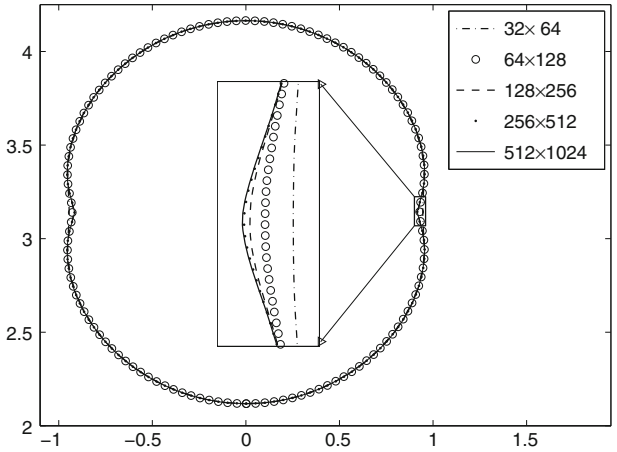

Fig. 13 Convergence of numerical results with refined spatial and temporal grids

$\Delta t = 0.75h^2$. Calculations are run up to time $T = 9.04$. In Fig. 12, we observe that without the interpolation, the shape of cell suffers from poor resolution, while with the interpolation, we have well resolved immersed boundary of the cell.

4.3 Convergence test

In this experiment, a numerical convergence test of cell growth is performed with grids $h = \pi/2^n$, and time steps, $\Delta t = 0.05 \times 2^{n-5}h^2$ up to the time $T = 0.904$ on the computational domain $\Omega = (0, \pi) \times (-\pi, \pi)$ for $n = 5, \ldots, 9$. The parameters $\mu = 0.2, \sigma_1 = 0.05, \epsilon = 0.01$, and $\alpha = 0.02$ are employed. Note that we use the same immersed boundary points $M = 2048$ in this numerical test. As shown in Fig. 13, the convergence of the results under spatial and temporal refinements is evident.

Table 1 Error and convergence results with various mesh grids

Case	32×64 (64×128)	Rate	64×128 (128×256)	Rate	128×256 (256×512)	Rate	256×512 (512×1024)
l_2	1.87E−3	1.63	6.07E−4	1.83	1.70E−4	1.73	5.13E−5

Here 32×64 (64×128) means $\|e_{h/\frac{h}{2}}\|_2$ with $h = \pi/32$

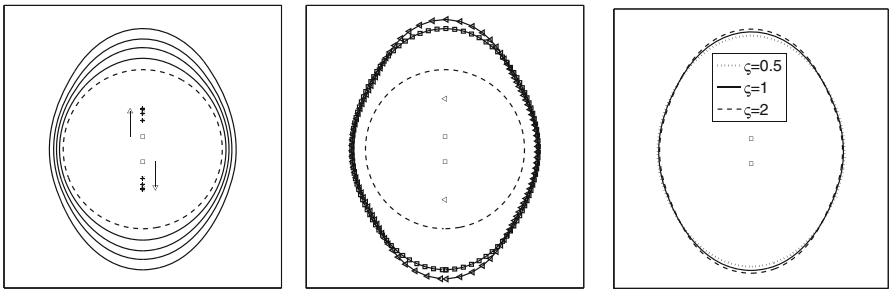

Fig. 14 Effect of source positions and strengths. **a** The evolution of cell growth by the position of two sources $\boldsymbol{Y}_1 = (0, -0.079)$ and $\boldsymbol{Y}_2 = (0, 0.079)$. **b** The comparison of final cell shapes with initial source positions. **c** The comparison of final cell shapes with different source strengths

Since there is no analytical solution, we define the error of the boundary location as the discrete l_2-norm of the distance between the points in the successively finer grids: $e_{h/\frac{h}{2},l} = |\mathbf{X}_{h,l} - \mathbf{X}_{h/2,l}|$. The rate of convergence is defined as the ratio of successive errors: $\log_2(\|e_{h/\frac{h}{2}}\|_2 / \|e_{\frac{h}{2}/\frac{h}{4}}\|_2)$, where the discrete l_2-norm is defined as $\|e_{h/\frac{h}{2}}\|_2 = \sqrt{\frac{1}{M}\sum_{l=1}^{M} e^2_{h/\frac{h}{2},l}}$. Using these definitions, the errors and rates of convergence are given in Table 1. The results suggest that the convergence rate with respect to spatial and temporal refinements is higher than the first order as we expect from the first order time stepping numerical scheme.

4.4 Effect of source positions and strengths

In Fig. 14, we show the effect of source positions for the cell growth. The numerical experiments are set on the computational domain $\Omega = (0, \pi) \times (-\pi, \pi)$ with the 64×128 mesh grids. We also take $\Delta t = h^2$ and $\sigma_1 = 0.02$ with the initial unit spherical shape (dashed line). We run the simulation until the volume of cell is doubled. Figure 14a shows the evolution of cell growth with two moving sources. The initial source positions are open square boxes with $d = 0.05\pi$. The arrows inside the cell show the directions of the moving two sources. In Fig. 14b, we consider two different source positions; open square box ($d = 0.05\pi$) and triangle symbol ($d = 0.2\pi$). The final shapes of cell are plotted with corresponding initial position symbols. It was found numerically that the relation between location of sources and the final cell shape elongation is nonlinear. Moreover, we consider the source strength, ς. The final

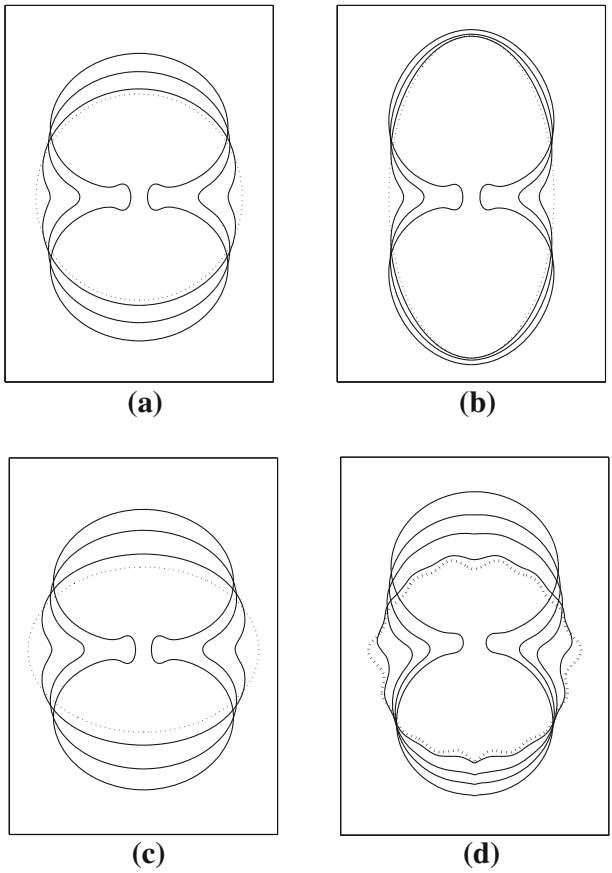

Fig. 15 The simulations with the different initial shapes marked with *dashed*. **a**–**c** The simulation with the initial shapes as *circle, short oval*, and *lager oval*, respectively. **d** The complex case drawn in Fig. 7a

shapes with $\varsigma = 0.5$, $\varsigma = 1$, and $\varsigma = 2$ are shown in Fig. 14c. We observe that as ς increases, the elongation goes further.

4.5 Effect of initial cell shapes

In this section, we claim that our proposed method for cell growth works well for different initial cell shapes. Numerical simulations are performed to demonstrate this claim. $\Delta t = 0.75h^2$, $\mu = 0.2$, $\sigma_1 = 0.05$, $\alpha = 0.03$, and $\epsilon = 0.01$ are used on the domain $(0, \pi) \times (-\pi, \pi)$ with 64×128 mesh grids. Four different initial cell shapes are tested: $a = 1$ and $b = 1$ (Fig. 15a), $a = 0.8$ and $b = 1.563$ (Fig. 15b), $a = 1.118$ and $b = 0.8$ (Fig. 15c), and complex cell shape in Fig.7a (Fig. 15d), respectively. Here $\boldsymbol{Y}_1 = (0, -0.157)$ and $\boldsymbol{Y}_2 = (0, 0.157)$ are used. These results suggest that our proposed mathematical model is robust in applying the stimulus algorithm to various cell shapes.

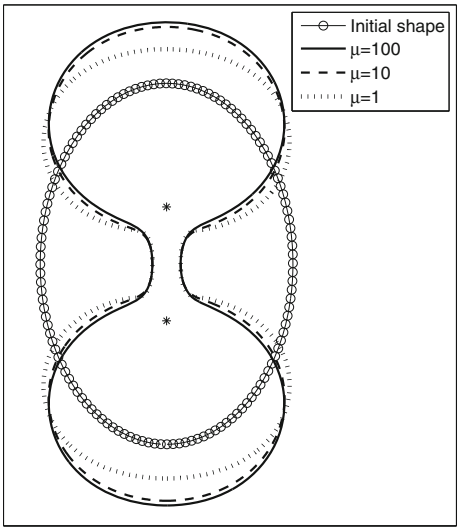

Fig. 16 Effect of μ with three different values of $\mu = 1,\ 10,\ 100$

4.6 Effect of viscosity μ

In this experiment, we investigate the effect of viscosity μ for the simulation of cell growth and division with three different values of $\mu = 1,\ 10,\ 100$. The initial cell shape is the unit circle on the domain $\Omega = (0, \pi) \times (-\pi, \pi)$ with the 64×128 mesh grids, and astral centers $\boldsymbol{Y}_1 = (0, -0.314)$ and $\boldsymbol{Y}_2 = (0, 0.314)$. We take $\Delta t = 0.02h^2$, $\sigma_1 = 1, \epsilon = 0.3$, and $\alpha = 2$ for the parameters. From the results shown in Fig. 16, we observe that the larger μ makes the daughter cell more spherical shape. When the viscosity is large, the inertia force is negligible, therefore the fluid system becomes Stokes flow which makes the cell shapes spherical.

4.7 Effect of control parameter ϵ

In Fig. 17, a computational experiment is performed to study the effect of control parameter ϵ during the cell division. The domain $\Omega = (0, \pi) \times (-\pi, \pi)$ with the 64×128 mesh grids, $\Delta t = 0.5h^2, \mu = 0.25, \sigma_1 = 0.05$, and $\alpha = 0.03$ are used with the initial condition $a = b = 1$. Here $\boldsymbol{Y}_1 = (0, -0.157)$ and $\boldsymbol{Y}_2 = (0, 0.157)$ are used. Figure 17 shows that intercellular bridge is getting longer with respect to the increasing values of ϵ. This conclusion has been investigated experimentally in biological process of cytokinesis by Gabriel et al. (2006).

4.8 Comparison with the experimental data

Finally, we compare our numerical simulation with experimental data in Boucrot and Kirchhausen (2007). The physical parameters in computational experiment are from the following references: viscosity $\mu = 100$ g/(cm s) (Laurent et al. 2003; Rejniak

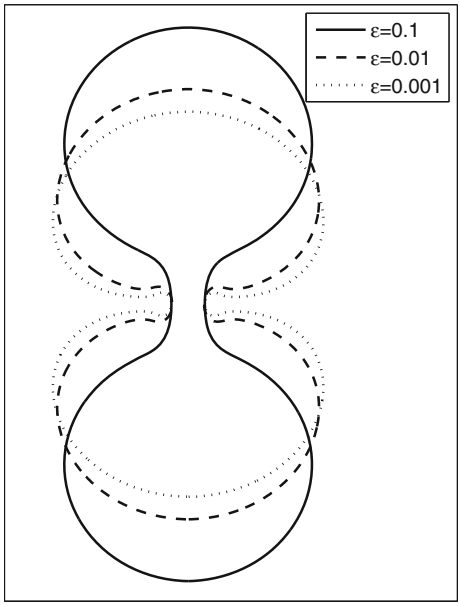

Fig. 17 The finial shape with three different control ϵ values

2005, 2007; Rejniak and Anderson 2008), density $\rho = 1.35$ g/(cm^3) (Dembo and Harlow 1986; Rejniak 2005, 2007; Rejniak and Anderson 2008), and the average diameter of cell 10 μm (Rejniak 2005, 2007; Rejniak and Anderson 2008). It should be pointed that since there is no real physical parameters for stiffness coefficients σ_1 and α, we simply choose those computational parameters as $\sigma_1 = 5 \times 10^6$ g/s^2 and $\alpha = 1 \times 10^7$ g/s^2 in order to get the appropriate numerical results and to match the experimental data. Furthermore, we set $\epsilon = 0.3$ on the computational domain $\Omega = (0, 10\ \mu\text{m}) \times (-10\ \mu\text{m}, 10\ \mu\text{m})$ with a 64×128 mesh. Calculation is run up to time $T = 0.688$ s with a time step $\Delta t = 1.22 \times 10^{-5}$ s. Here, $\boldsymbol{Y}_1 = (0, -1\ \mu\text{m})$ and $\boldsymbol{Y}_2 = (0, 1\ \mu\text{m})$ are used. For the initial cell shape, we use the image segmentation algorithm in Li and Kim (2010) to get the edges of the cell. Figure 18a is the evolution of cell division and the arrows show the direction of the evolution. Figure 18b–d are the overlapped simulations of cell division by comparing with the experiment data. These results demonstrate that our computational results are in good qualitative agreement with the experimental data.

5 Conclusion and discussion

In this paper, we have presented a mathematical modeling with an efficient and accurate numerical method to investigate morphological transition while an animal cell undergoes cytokinesis. The proposed model is robust and realistic in locating the position of the cleavage furrow and in applying the contractile force. We have used an immersed boundary method to numerically track the morphology of cell membrane during the cytokinesis. For numerical approaches, we have employed an adaptive

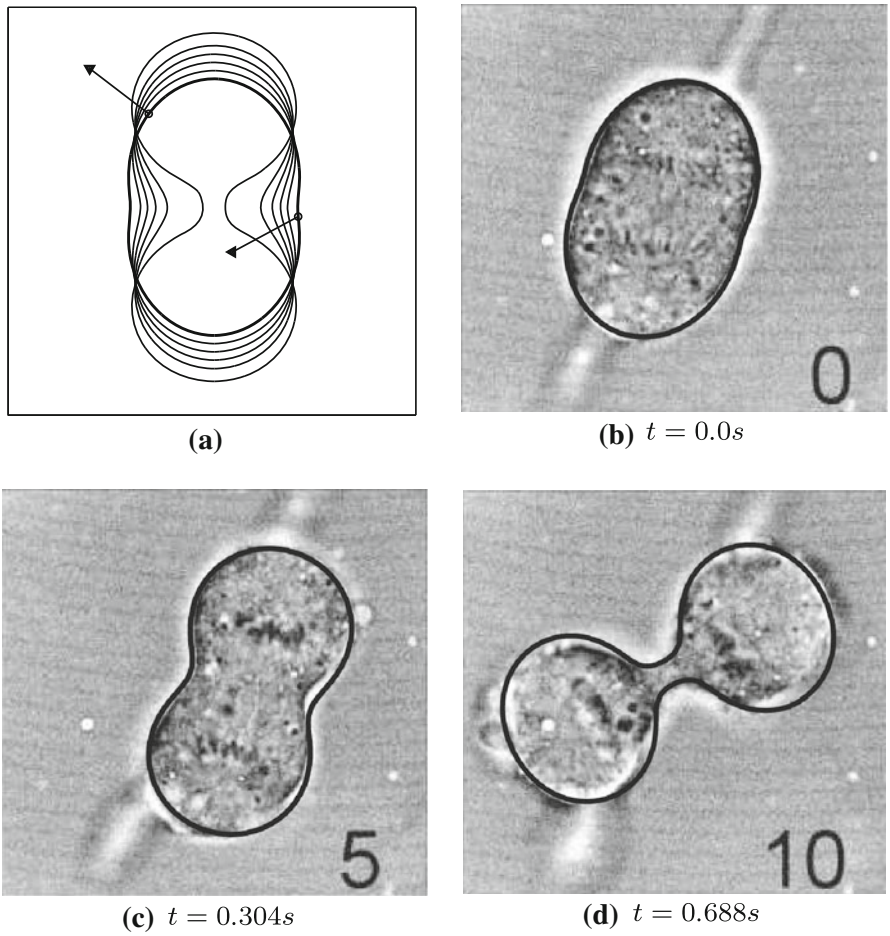

(a) **(b)** $t = 0.0s$ **(c)** $t = 0.304s$ **(d)** $t = 0.688s$

Fig. 18 **a** Evolution of cell division. **b–d** The overlapped simulations of cell division by comparing with the experiment data

immersed boundary method to have efficient and accurate results. We have performed numerical simulations on the axisymmetric domain to use sufficient resolution and to see three-dimensional effects such as anisotropic surface tensions. We also have investigated the effects of each model parameter and have compared a numerical result with the experimental data.

We have presented here a simple mathematical model in axisymmetric domain. But as the axisymmetric model has physical limitation, that is, direction of the cell division process is limited, we are currently working on a fully three-dimensional single cell model to investigate the more realistic cell division process. In the immersed boundary method, the pinch-off process is performed when the opposite boundary points are within a small distance (Rejniak and Anderson 2008). This pinch-off process is more or less numerical technique. We need to develop more realistic pinch-off process. For this purpose, we are currently working on a hybrid method, where the immersed

boundary method and the phase-field method are combined to simulate the topological transition smoothly.

Finally, when the cell-to-cell interactions and a lifespan of the cell are considered, the multicelluar model can be modeled, like previous other authors' work (Rejniak 2007; Rejniak and Anderson 2008; Dillon et al. 2007; Shirinifard et al. 2009). For the future work, we will incorporate theses cell-to-cell interactions in our model for the growth and division process of the tissue cells.

Acknowledgments This research was supported by Basic Science Research Program through the National Research Foundation of Korea (NRF) funded by the Ministry of Education, Science and Technology (No. 2010-0003989). The authors also wish to thank the reviewers for the constructive and helpful comments on the revision of this article.

Appendix

The algorithm of our proposed method will be described as following steps:

Step 1. Find the force $\boldsymbol{f}^n$ on the immersed boundary from the given boundary configuration $\boldsymbol{X}^n$.

$$\begin{aligned} \boldsymbol{f}_l^n &= (\sigma_1 \kappa_{1l} + \sigma_2(s,t)\kappa_{2l})\,\boldsymbol{n}_l \quad \text{for } l = 1, \ldots, M, \\ \sigma_2(s,t) &= \frac{\alpha H(t-t_0)}{\big||\boldsymbol{X}_l - \boldsymbol{Y}_1| - |\boldsymbol{X}_l - \boldsymbol{Y}_2|\big| + \epsilon} + \sigma_1(1 - H(t-t_0)) \\ \kappa_{1l} &= \frac{(R_s^n)_l (Z_{ss}^n)_l - (R_{ss}^n)_l (Z_s^n)_l}{\sqrt{(R_s^n)_l^2 + (Z_s^n)_l^2}^3}, \quad \kappa_{2l} = \frac{(Z_s^n)_l}{R_l^n \sqrt{(R_s^n)_l^2 + (Z_s^n)_l^2}}, \end{aligned}$$

where $\boldsymbol{n}_l = (m_l, n_l)$ is the unit normal vector and calculated by using three points $\boldsymbol{X}_{l-1}$, $\boldsymbol{X}_l$, and $\boldsymbol{X}_{l+1}$ with the following quadratic polynomial approximations.

$$R(t) = \alpha_1 t^2 + \beta_1 t + \gamma_1 \quad \text{and} \quad Z(t) = \alpha_2 t^2 + \beta_2 t + \gamma_2.$$

Assume $\boldsymbol{X}_{l-1} = (R(0), Z(0))$, $\boldsymbol{X}_l = (R(\Delta s_l), Z(\Delta s_l))$, and $\boldsymbol{X}_{l+1} = (R(\Delta s_l + \Delta s_{l+1}), Z(\Delta s_l + \Delta s_{l+1}))$, then the parameters α_1, β_1, and γ_1 can be calculated by the following equations.

$$\begin{pmatrix} \alpha_1 \\ \beta_1 \\ \gamma_1 \end{pmatrix} = \begin{pmatrix} 0 & 0 & 1 \\ \Delta s_l^2 & \Delta s_l & 1 \\ (\Delta s_l + \Delta s_{l+1})^2 & \Delta s_l + \Delta s_{l+1} & 1 \end{pmatrix}^{-1} \begin{pmatrix} R(0) \\ R(\Delta s_l) \\ R(\Delta s_l + \Delta s_{l+1}) \end{pmatrix}.$$

α_2, β_2, and γ_2 are calculated similarly. Now we get the unit normal vector as

$$\boldsymbol{n}_l = \left(\frac{\frac{dZ(\Delta s_l)}{dt}}{\sqrt{\left(\frac{dR(\Delta s_l)}{dt}\right)^2 + \left(\frac{dZ(\Delta s_l)}{dt}\right)^2}}, \frac{-\frac{dR(\Delta s_l)}{dt}}{\sqrt{\left(\frac{dR(\Delta s_l)}{dt}\right)^2 + \left(\frac{dZ(\Delta s_l)}{dt}\right)^2}} \right).$$

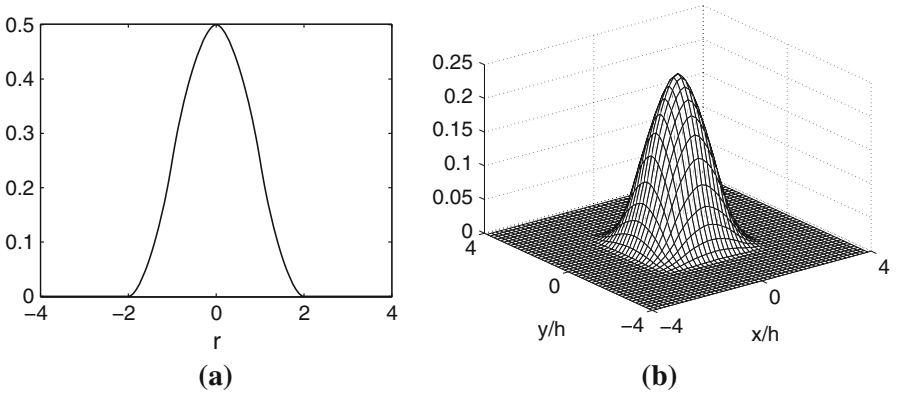

Fig. 19 **a** One- and **b** two-dimensional Dirac delta functions

And also for $(R_s^n)_l$ and $(R_{ss}^n)_l$, we use the following discretization:

$$(R_s^n)_l = \left(\frac{\Delta s_l^n (R_{l+1}^n - R_l^n)}{2\Delta s_{l+1}^n} + \frac{\Delta s_{l+1}^n (R_l^n - R_{l-1}^n)}{2\Delta s_l^n} \right) \Big/ \Delta s_{l+1/2}^n,$$

$$(R_{ss}^n)_l = \left(\frac{R_{l+1}^n - R_l^n}{\Delta s_{l+1}^n} - \frac{R_l^n - R_{l-1}^n}{\Delta s_l^n} \right) \Big/ \Delta s_{l+1/2}^n,$$

where $\Delta s_{l+1/2}^n = (\Delta s_l^n + \Delta s_{l+1}^n)/2$.

Step 2. Spread the boundary force into the nearby grid points of the fluid.

$$\boldsymbol{F}_{ik}^n = \sum_{l=1}^{M} \boldsymbol{f}_l^n \delta_h^2 (\boldsymbol{x}_{ik} - \boldsymbol{X}_l^n) \Delta s_{l+1/2}^n \quad \text{for } i = 1, \ldots, N_r \text{ and } k = 1, \ldots, N_z,$$

where δ_h^2 is a smoothed approximation to the two-dimensional Dirac delta function:

$$\delta_h^2(\boldsymbol{x}) = \frac{1}{h^2} \phi\left(\frac{r}{h}\right) \phi\left(\frac{z}{h}\right),$$

where

$$\phi(x) = \begin{cases} \left(3 - 2|x| + \sqrt{1 + 4|x| - 4x^2}\right)/8 & \text{if } |x| \le 1, \\ \left(5 - 2|x| - \sqrt{-7 + 12|x| - 4x^2}\right)/8 & \text{if } 1 < |x| \le 2, \\ 0 & \text{if } 2 < |x|. \end{cases}$$

One- and two-dimensional Dirac delta functions are shown in Fig. 19. The motivation for this particular choice of $\phi(x)$ is given in Peskin and Mcqueen (1995).

Step 3. Solve the Navier–Stokes equations Eqs. (2) and (3) on the rectangular grid to get $\boldsymbol{u}^{n+1}$ and p^{n+1} from $\boldsymbol{u}^n$ and $\boldsymbol{F}^n$:

$$\rho\left(\frac{u^{n+1}-u^n}{\Delta t}+u^n u_r^n+w^n u_z^n\right)=-p_r^{n+1}+\mu\left[\frac{1}{r}(ru_r^n)_r+u_{zz}^n-\frac{u^n}{r^2}\right]+\frac{\mu}{3\rho}S_r^n+F_1^n, \tag{15}$$

$$\rho\left(\frac{w^{n+1}-w^n}{\Delta t}+u^n w_r^n+w^n w_z^n\right)=-p_z^{n+1}+\mu\left[\frac{1}{r}(rw_r^n)_r+w_{zz}^n\right]+\frac{\mu}{3\rho}S_z^n+F_2^n, \tag{16}$$

$$\rho\nabla_d\cdot\boldsymbol{u}^{n+1}=S^n. \tag{17}$$

Where $\boldsymbol{S}^n=(S_r^n,S_z^n)=\sum_{j=1}^{2}S_j^n\delta^2(\boldsymbol{x}_{ik}-\boldsymbol{Y}_j^n)$ and S_j^n is ς until the mass of cell is double, and S_j^n is zero when $t\geq t_0$.

First, solve an intermediate velocity field, $\tilde{\boldsymbol{u}}$, which does not satisfy the incompressible condition, without the pressure gradient term,

$$\rho\left(\frac{\tilde{u}-u^n}{\Delta t}+u^n u_r^n+w^n u_z^n\right)=\mu\left[\frac{1}{r}(ru_r^n)_r+u_{zz}^n-\frac{u^n}{r^2}\right]+\frac{\mu}{3\rho}S_r^n+F_1^n,$$

$$\rho\left(\frac{\tilde{w}-w^n}{\Delta t}+u^n w_r^n+w^n w_z^n\right)=\mu\left[\frac{1}{r}(rw_r^n)_r+w_{zz}^n\right]+\frac{\mu}{3\rho}S_z^n+F_2^n,$$

The resulting finite difference equations are written out explicitly. They take the form

$$\tilde{u}_{i+\frac{1}{2},k}=u_{i+\frac{1}{2},k}^n-\Delta t(uu_r+wu_z)_{i+\frac{1}{2},k}^n+\frac{\mu}{3\rho^2 h}(S_{i+1,j}^n-S_{i,j}^n)+\frac{\Delta t}{\rho}F_{i+\frac{1}{2},k}^{r-edge}+\frac{\mu\Delta t}{\rho}\left(\frac{r_{i+\frac{1}{2}}\left(u_{i+\frac{3}{2},k}^n-u_{i+\frac{1}{2},k}^n\right)-r_{i-\frac{1}{2}}\left(u_{i+\frac{1}{2},k}^n-u_{i-\frac{1}{2},k}^n\right)}{r_i h^2}-\frac{u_{i+\frac{1}{2},k}^n}{r_i^2}+\frac{u_{i+\frac{1}{2},k+1}^n-2u_{i+\frac{1}{2},k}^n+u_{i+\frac{1}{2},k-1}^n}{h^2}\right), \tag{18}$$

$$\tilde{w}_{i,k+\frac{1}{2}}=w_{i,k+\frac{1}{2}}^n-\Delta t(uw_r+ww_z)_{i,k+\frac{1}{2}}^n+\frac{\mu}{3\rho^2 h}(S_{i,j+1}^n-S_{i,j}^n)+\frac{\Delta t}{\rho}F_{i,k+\frac{1}{2}}^{z-edge}+\frac{\mu\Delta t}{\rho}\left(\frac{r_{i+\frac{1}{2}}\left(w_{i+1,k+\frac{1}{2}}^n-w_{i,k+\frac{1}{2}}^n\right)-r_{i-\frac{1}{2}}\left(w_{i,k+\frac{1}{2}}^n-w_{i-1,k+\frac{1}{2}}^n\right)}{r_i h^2}+\frac{w_{i,k+\frac{3}{2}}^n-2w_{i,k+\frac{1}{2}}^n+w_{i,k-\frac{1}{2}}^n}{h^2}\right), \tag{19}$$

where the advection terms, $(uu_r + wu_z)^n_{i+\frac{1}{2},k}$ and $(uw_r + vw_z)^n_{i,k+\frac{1}{2}}$ are defined by

$$\begin{aligned}(uu_r + wu_z)^n_{i+\frac{1}{2},k} &= u^n_{i+\frac{1}{2},k}\bar{u}^n_{r_{i+\frac{1}{2},k}} \\ &\quad + \frac{w^n_{i,k-\frac{1}{2}} + w^n_{i+1,k-\frac{1}{2}} + w^n_{i,k+\frac{1}{2}} + w^n_{i+1,k+\frac{1}{2}}}{4}\bar{u}^n_{z_{i+\frac{1}{2},k}}, \\ (uw_r + ww_z)^n_{i,k+\frac{1}{2}} &= w^n_{i,k+\frac{1}{2}}\bar{w}^n_{z_{i,k+\frac{1}{2}}} \\ &\quad + \frac{u^n_{i-\frac{1}{2},k} + u^n_{i-\frac{1}{2},k+1} + u^n_{i+\frac{1}{2},k} + u^n_{i+\frac{1}{2},k+1}}{4}\bar{w}^n_{r_{i,k+\frac{1}{2}}}.\end{aligned}$$

The values $\bar{u}^n_{r_{i+\frac{1}{2},k}}$ and $\bar{u}^n_{z_{i+\frac{1}{2},k}}$ are computed by using the upwind procedure. The procedure is

$$\bar{u}^n_{r_{i+\frac{1}{2},k}} = \begin{cases} (u^n_{i+\frac{1}{2},k} - u^n_{i-\frac{1}{2},k})/h & \text{if } u^n_{i+\frac{1}{2},k} > 0 \\ (u^n_{i+\frac{3}{2},k} - u^n_{i+\frac{1}{2},k})/h & \text{otherwise} \end{cases}$$

and

$$\bar{u}^n_{z_{i+\frac{1}{2},k}} = \begin{cases} (u^n_{i+\frac{1}{2},k} - u^n_{i+\frac{1}{2},k-1})/h & \text{if } w^n_{i,k-\frac{1}{2}} + w^n_{i+1,k-\frac{1}{2}} + w^n_{i,k+\frac{1}{2}} + w^n_{i+1,k+\frac{1}{2}} > 0 \\ (u^n_{i+\frac{1}{2},k+1} - u^n_{i+\frac{1}{2},k})/h & \text{otherwise.} \end{cases}$$

The quantities $\bar{w}^n_{r_{i,k+\frac{1}{2}}}$ and $\bar{w}^n_{z_{i,k+\frac{1}{2}}}$ are computed in a similar manner. Then, we solve the following equations for the advanced pressure field at $(n+1)$ time step.

$$\rho\frac{\boldsymbol{u}^{n+1} - \tilde{\boldsymbol{u}}}{\Delta t} = -\nabla_d p^{n+1}, \tag{20}$$

$$\rho\nabla_d \cdot \boldsymbol{u}^{n+1} = S^n. \tag{21}$$

With application of the divergence operator to Eq. (20), we find that the Poisson equation for the pressure at the advanced time $(n+1)$.

$$\Delta_d p^{n+1} = \frac{1}{\Delta t}\left(\rho\nabla_d \cdot \tilde{\boldsymbol{u}} - S^n\right), \tag{22}$$

where we have substituted Eq. (21). The terms are defined as the following:

$$\begin{aligned}\Delta_d p^{n+1}_{ik} &= \frac{r_{i+\frac{1}{2}}(p^{n+1}_{i+1,k} - p^{n+1}_{ik}) - r_{i-\frac{1}{2}}(p^{n+1}_{ik} - p^{n+1}_{i-1,k})}{r_i h^2} \\ &\quad + \frac{p^{n+1}_{i,k+1} - 2p^{n+1}_{ik} + p^{n+1}_{i,k-1}}{h^2}, \\ \nabla_d \cdot \tilde{\boldsymbol{u}}_{ik} &= \frac{r_{i+\frac{1}{2}}\tilde{u}_{i+\frac{1}{2},k} - r_{i-\frac{1}{2}}\tilde{u}_{i-\frac{1}{2},k}}{r_i h} + \frac{\tilde{w}_{i,k+\frac{1}{2}} - \tilde{w}_{i,k-\frac{1}{2}}}{h}.\end{aligned}$$

The resulting linear system Eq. (22) is solved using a multigrid method, specifically, V-cycles with a Gauss–Seidel relaxation. Then the updated velocities u^{n+1} and w^{n+1} are defined by

$$\boldsymbol{u}^{n+1} = \tilde{\boldsymbol{u}} - \frac{\Delta t}{\rho}\nabla_d p^{n+1}, \text{ that is,}$$
$$u^{n+1}_{i+\frac{1}{2},k} = \tilde{u}_{i+\frac{1}{2},k} - \frac{\Delta t}{\rho h}(p_{i+1,k} - p_{ik}),\ w^{n+1}_{i,k+\frac{1}{2}} = \tilde{w}_{i,k+\frac{1}{2}} - \frac{\Delta t}{\rho h}(p_{i,k+1} - p_{ik}).$$

Step 4. Once the updated fluid velocity $\boldsymbol{u}^{n+1}$, has been determined, we can find the velocity on the immersed boundary $\boldsymbol{U}^{n+1}$, with these, then we have the new immersed boundary points $\boldsymbol{X}^{n+1}$, and the new center positions, $\boldsymbol{Y}^{n+1}$. This is done using a discretization of Eqs. (8)–(11). The difference approximations to the interpolation equation are expressed as follows:

$$\boldsymbol{U}_l^{n+1} = \sum_{i=0}^{N_r-1}\sum_{k=0}^{N_z-1} \boldsymbol{u}_{ik}^{n+1}\delta_h^2(\boldsymbol{x}_{ik} - \boldsymbol{X}_l^n)h^2 \quad \text{for } l = 1, \ldots, M, \tag{23}$$
$$\boldsymbol{X}_l^{n+1} = \boldsymbol{X}_l^n + \Delta t \boldsymbol{U}_l^{n+1}, \tag{24}$$
$$\boldsymbol{U}_j^{n+1} = \sum_{i=0}^{N_r-1}\sum_{k=0}^{N_z-1} \boldsymbol{u}_{ik}^{n+1}\delta_h^2(\boldsymbol{x}_{ik} - \boldsymbol{Y}_j^n)h^2 \quad \text{for } j = 1, 2, \tag{25}$$
$$\boldsymbol{Y}_j^{n+1} = \boldsymbol{Y}_j^n + \Delta t \boldsymbol{U}_j^{n+1}, \tag{26}$$

where $\boldsymbol{u}_{ik}^{n+1} = ((u_{i-1/2,k}^{n+1} + u_{i+1/2,k}^{n+1})/2, (w_{i,k-1/2}^{n+1} + w_{i,k+1/2}^{n+1})/2)$.

Following the *Step* 1–*Step* 4, one iteration of computational simulation is completed.

During the simulation, some interfaces are stretched and some are compressed. To accurately and efficiently calculate interface forces, we need uniformly distributed immersed boundary points. In this section, we present a numerical algorithm which adds and deletes points during the simulation.

For an interval size with $\Delta s_{l+1} > 0.5h$, we insert a boundary point $\boldsymbol{X}_* = 0.5(\bar{\boldsymbol{X}}_1 + \bar{\boldsymbol{X}}_2)$. Here $\bar{\boldsymbol{X}}_j$ $(j = 1, 2)$ are calculated by using three points $\boldsymbol{X}_{l+j-2}$, $\boldsymbol{X}_{l+j-1}$, and $\boldsymbol{X}_{l+j}$ with the quadratic polynomial approximation. Let the quadratic polynomial approximation for the three points $\boldsymbol{X}_{l-1}$, $\boldsymbol{X}_l$, and $\boldsymbol{X}_{l+1}$ be

$$R(t) = \alpha_1 t^2 + \beta_1 t + \gamma_1, \text{ and } Z(t) = \alpha_2 t^2 + \beta_2 t + \gamma_2.$$

We define

$$\bar{\boldsymbol{X}}_1 = (R(\Delta s_l + 0.5\Delta s_{l+1}), Z(\Delta s_l + 0.5\Delta s_{l+1}))\,.$$

$\bar{\boldsymbol{X}}_2$ is similarly calculated. In case of the given position $\boldsymbol{X}_l$ satisfies that $\Delta s_l + \Delta s_{l+1} < 0.25h$, we delete this position from the surface boundary in order to get the effectiveness and robustness in our computational experiments.

References

Barr FA, Gruneberg U (2007) Cytokinesis: placing and making the final cut. Cell 131:847–860

Bernoff AJ, Bertozzi AL, Witelski TP (1998) Axisymmetric surface diffusion: dynamics and stability of self-similar pinchoff. J Stat Phys 93(3/4):725–776

Boucrot E, Kirchhausen T (2007) Endosomal recycling controls plasma membrane area during mitosis. Proc Natl Acad Sci USA 104(19):7939–7944

Dembo M, Harlow F (1986) Cell motion, contractile networks, and the physics of interpenetrating reactive flow. Biophys J 50:109–121

Devore JJ, Conrad GW, Rappaport R (1989) A model for astral stimulation of cytokinesis in animal cells. J Cell Biol 109:2225–2232

Dillon MF, McDermott EW, O'Doherty A, Quinn CM, Hill AD, O'Higgins N (2007) Factors affecting successful breast conservation for ductal carcinoma in situ. Ann Surg Oncol 14(5):1618–1628. doi:10.1245/s10434-006-9246-y

Gabriel M, Kopecka M, Yamaguchi M, Svoboda A, Takeo K, Yoshida S, Ohkusu M, Sugita T, Nakase T (2006) Cytoskeleton in the unique cell reproduction by conidiogenesis of the long neck yeast Fellomyces (Sterigmatomyces) fuzhouensis. Protoplasma 229:33–44

Greenspan HP (1977) On the dynamics of cell cleavage. J Theor Biol 65:79–99

Guertin DA, Trautmann S, McCollum D (2002) Cytokinesis in eukaryotes. Microbiol Mol Biol Rev 66:155–178

Guyon E, Hulin JP, Petit L, Mitescu CD (2001) Physical hydrodynamics. Oxford University Press, Oxford

Harlow F, Welch J (1965) Numerical calculations of time dependent viscous incompressible flow with free surface. Phys Fluids 8:2182–2189

Hilbing JH, Heister SD, Spangler CA (1995) A boundary-element method for atomization of a finite liquid jet. Atomization Sprays 15:621–638

Lai MC, Huang CY, Huang YM (2004) Simulating the axisymmetric interfacial flows with insoluble surfactant by immersed boundary method. Int J Num Anal Mod 1(1):1–18

Laurent VM, Planus E, Fodil R, Isabey D (2003) Mechanical assessment by magnetocytometry of the cytosolic and cortical cytoskeletal compartments in adherent epithelial cells. Biology 40:235–240

Li YB, Kim JS (2010) A fast and accurate numerical method for medical image segmentation. J KSIAM 14(4):201–210

Murray JD, Oster GF, Harris AK (1983) A mechanical model for mesenchymal morphogenesis. J Math Biol 17:125–129

Oegema K, Mitchison TJ (1997) Cleavage furrow induction in animal cells. Proc Natl Acad Sci USA 94:4817–4820

Peskin CS, Mcqueen DM (1995) A general method for the computer simulation of biological systems interacting with fluids. Symp Soc Exp Biol 49:265–276

Rappaport R (1986) Establishment of the mechanism of cytokinesis in animal cells. Int Rev Cytol 105:245–281

Rejniak KA (2005) A single-cell approach in modeling the dynamics of tumor microregions. Math Biosci Eng 2:643–655

Rejniak KA (2007) An immersed boundary framework for modelling the growth of individual cells: an application to the early tumour development. J Theor Biol 247:186–204

Rejniak KA, Anderson ARA (2008) A computational study of the development of epithelial acini: I. Sufficient conditions for the formation of a hollow structure. Bull Math Biol 70(3):677–712

Satterwhite LL, Pollard TD (1992) Cytokinesis. Curr Opin Cell Biol 4:43–52

Shirinifard A, Gens JS, Zaitlen BL, Poplawski NJ, Swat M, Glazier JA (2009) 3D Multi-cell simulation of tumor growth and angiogenesis. PLoS ONE 4:e7190

Tyson JJ, Hannsgen KB (1986) Cell growth and division: a deterministic/probabilistic model of the cell cycle. J Math Biol 23:231–246

White JG, Borisy GG (1983) On the mechanisms of cytokinesis in animal cells. J Theor Biol 101:289–316

Wolpert L (1960) The mechanics and mechanism of cleavage. Int Rev Cytol 10:163–216